



# Ionic covalent organic nanosheet anchoring discrete copper for efficient quasi-homogeneous photocatalytic proton reduction

Ying Zang, Yuan-Jie Cheng, Zhao-Di Wang, Peng Peng, Qing-Guo Dong, Hong Chen, Rui Wang\*, Shuang-Quan Zang\*

Henan Key Laboratory of Crystalline Molecular Functional Materials, Henan International Joint Laboratory of Tumor Theranostical Cluster Materials, Green Catalysis Center, and College of Chemistry, Zhengzhou University, Zhengzhou 450001, China

## ARTICLE INFO

### Keywords:

Covalent organic nanosheet  
Heterogeneous catalysis  
Discrete copper  
Photocatalysis  
Proton reduction

## ABSTRACT

Covalent organic nanosheets can be applied potentially to solar-to-hydrogen fuel conversion because of their long-range ordered structure and predictable regulation. Additionally, minor progress has been made in the precise synthesis of copper-loaded composite catalysts at the atomic level. Hence, we synthesized hybrid Cu@TpTG-iCON materials by anchoring copper(II) ions into the evenly dispersed tridentate chelation sites of the TpTG-iCON precursor, which maximized the exposure of active sites during the catalytic reaction. Taking advantage of the well-defined structural configuration and nanosheet morphology, the heterogeneous Cu@TpTG-iCON catalyst exhibited an excellent hydrogen evolution reaction (HER) rate and significant stability in a ternary photocatalytic system. The atomic-level coordination modulation strategy in the covalent organic nanosheet matrix successfully demonstrated here has made possible the synthesis of other non-precious metal-based hybrid materials, indicating a step forward in the generation of a recyclable and efficient HER catalyst.

## 1. Introduction

The photochemical conversion of solar energy to non-polluted fuels has long been studied due to the high demand for a future clean and sustainable energy society [1]. Hydrogen, as a clean energy carrier with high energy density, is the most available renewable energy [2]. Photocatalytic proton reduction for H<sub>2</sub> evolution is one of the most appealing solutions for energy storage and green production of hydrogen fuel and has attracted widespread attention [3–7]. Although platinum (Pt)-based catalysts have shown satisfactory activity in catalysing proton reduction, the high material cost and scarce reserves inevitably limit their large-scale application [8]. To overcome these drawbacks, various strategies for constructing non-precious metal-based catalytic materials have been proposed [9–11]. Over the past few decades, despite the reported Cu-based coordination polymer has shown significant catalytic reactivity [7,9], copper-based catalysts for the photocatalytic HER have still received less attention than other intensively studied transition metals (Fe [12], Co [13], Ni [14], etc.) photocatalysts. Very recently, Lu and co-workers impressively proposed a novel hybrid photocatalyst containing linkers with transient Cu centers, which boosts the lifetime of the carrier density and photo-generated

charges to enhance photocatalytic HER activity [15].

In recent years, covalent organic frameworks (COFs) with the unique advantages of adjustable structures and electrical properties have been extensively studied for use in photocatalytic proton reduction [16–18]. More importantly, COF materials composed of only light elements (C, H, N, O, etc.) have great prospects as universal matrix platforms for the modular synthesis of heterogeneous supported catalysts [19]. Imine-linked COFs have abundant nitrogen atoms with lone pair electrons, which can fix and separate the metal atoms in a well-defined position, offering precise control of the arrangement of the active sites. Zhao and co-workers fabricated versatile hydrazone-linked COF-based materials to chelate different transition metal ions via the attached nitrogen sites, resulting in excellent catalytic activity for the Suzuki-Miyaura cross-coupling reaction [20]. Furthermore, rare and expensive platinum is frequently used as a co-catalyst and is incorporated into COF-based photocatalytic systems to reduce the overpotential of the HER [21,22], which seems to be the bottleneck that limits the economical solar HER system. Recently, Lotsch and co-workers reported a low-cost thiazolo[5,4-d]thiazole-linked COF-based hybrid photocatalyst anchoring the non-precious nickel thiolate cluster co-catalyst with excellent long-term HER performance [23], introducing a new

\* Corresponding authors.

E-mail addresses: [wangruijy@zzu.edu.cn](mailto:wangruijy@zzu.edu.cn) (R. Wang), [zangsqzg@zzu.edu.cn](mailto:zangsqzg@zzu.edu.cn) (S.-Q. Zang).

<https://doi.org/10.1016/j.apcatb.2021.120817>

Received 26 August 2021; Received in revised form 6 October 2021; Accepted 10 October 2021

Available online 12 October 2021

0926-3373/© 2021 Elsevier B.V. All rights reserved.

application of COFs as excellent catalyst supports for non-noble-metal-based photocatalytic HER systems.

The two-dimensional (2D) ultrathin nanosheet configuration with atomic-scale thickness and distinctive electronic states can decrease the carrier diffusion length to enhance the transfer rate of the reactive substrate and charge [24]. Furthermore, the large surface-to-volume ratio endows 2D nanosheets with abundant exposed sites, which are beneficial for chemical modification. The relatively weak non-covalent interactions in the out-of-plane direction allow the bulk COF to be stripped into 2D covalent organic nanosheets (CONs) [25]. In addition, CONs stacked in a few layers still maintain the characteristics of COFs, such as a tuneable coordination environment and excellent chemical stability [26]. 2D CONs with in-plane conjugate systems can exhibit high charge transferability, resulting in promising rapid transfer for photo-generated electrons, which promotes electron diffusion-controlled proton reduction processes [27]. Compared to neutral COF materials, which are unable to form layered nanosheets because of relatively strong  $\pi - \pi$  interactions, ionic COF materials exhibit charge repulsion between inbuilt layers that is expected to induce self-exfoliation of ionic covalent organic nanosheets (iCONs) [26, 28]. To date, little attention has been given to examining the HER performance of iCON-based hybrid catalysts due to the lack of efficient active sites.

In this work, we selected TpTG-iCON (Tp: 1,3,5-triformylphloroglucinol; TG: triaminoguanidinium chloride), which is formed by self-exfoliation as a support material, and utilized abundant nitrogen atoms with lone pairs for metal copper coordination via convenient post-modification synthesis. Finally, the iCON-based hybrid catalyst denoted Cu@TpTG-iCON, was obtained as a stable, efficient, and recyclable HER catalyst, showing a high hydrogen evolution rate of  $8484 \mu\text{mol g}^{-1} \text{h}^{-1}$  under irradiation over 10 h in the optimized photocatalytic system. The strong chelated coordination interaction between nitrogen atoms and copper ensures that the catalytic metal sites will not easily disengage from the nanosheet matrix, consequently enhancing the stability and recyclability of Cu@TpTG-iCON. The excellent catalytic activity is due to the few layers of nanosheet structures that expose more catalytic sites and accelerate the transfer speed of charges at the interface, which provides a future path to nonprecious catalyst renovations for clean hydrogen generation.

## 2. Experimental section

### 2.1. Synthesis of 1, 3, 5-triformylphloroglucinol (Tp)

Tp was synthesized according to the procedures described in the literature [29]. To Hexamethylenetetramine (15.1 g, 108 mmol) and 1, 3,5-Trihydroxybenzene (6.0 g, 49 mmol) under  $\text{N}_2$  was added 90 mL trifluoroacetic acid. The solution was heated to  $100^\circ\text{C}$  and maintained for ca. 2.5 h. With addition of 150 mL of 3 M HCl, the mixture was kept at  $100^\circ\text{C}$  for another 1 h. After cooling to room temperature, the solution was filtered, extracted with dichloromethane ( $4 \times 100$  mL), dried over anhydrous  $\text{Mg}_2\text{SO}_4$ , and filtered. Rotary evaporation of the solvent afforded the orange powder. The solid was repeatedly washed with hot ethanol to get a light pink powder (1.28 g, yield: 22%).  $^1\text{H}$  NMR (400 MHz,  $\text{CDCl}_3$ ):  $\delta$  (ppm) 14.16 (s, 3 H, OH), 10.19 (s, 3 H, CHO).

### 2.2. Synthesis of triaminoguanidinium chloride (TG)

Triaminoguanidinium chloride (TG) was synthesized using hydrazine hydrate in 1,4-dioxane under refluxing condition [30]. Briefly, 1.91 g of guanidine hydrochloride was added to 10 mL of 1,4-dioxane under stirring condition. With addition of 3.3 mL hydrazine hydrate, the mixture was refluxed at  $100^\circ\text{C}$  for 2 h. After cooling to room temperature, the solution was filtered and washed with 1,4-dioxane to remove excess hydrazine hydrate and finally dried to yield TG (4.2 g, yield: 98%).

### 2.3. Synthesis of TpTG-iCON

A mixture of Tp (42 mg) and TG (28 mg) in the mixed solvent of 2 mL 1,4-dioxane-mesitylene and 600  $\mu\text{L}$  deionized water was sonicated for 15 min, then 0.2 mL of 6 M acetic acid solution was added in succession at room temperature. Subsequently, the mixture was then sealed in a Teflon-lined stainless steel container and heated at  $120^\circ\text{C}$  for 72 h. After that we turn off the oven and the cooling process is implementing undisturbed. A brown precipitate was collected by filtration and washed with N,N-dimethylacetamide, deionized water and acetone thrice. The powder collected was then dried at  $100^\circ\text{C}$  under vacuum to get TpTG-iCON (Scheme S1).

### 2.4. Synthesis of Cu@TpTG-iCON

The  $\text{CuCl}_2 \cdot 2\text{H}_2\text{O}$  (102.3 mg) was dissolved in 10 mL ethanol to form a green solution A. 90.6 mg TpTG-iCON were dispersed in 10 mL ethanol to form a brown suspension B. Then the solution A was added in the suspension B with stirring for 12 h at room temperature. After that, the mixed solution was centrifuged and washed with ethanol until the filtrate was colourless. Repeated the above steps and the precipitate was dried in vacuum to give the Cu@TpTG-iCON (76 mg) (Scheme S2).

### 2.5. Photocatalytic hydrogen evolution of Cu@TpTG-iCON

The photocatalytic hydrogen production experiments and conditions optimization experiments were operated in a 60 mL closed quartz cell using the Perfect light photochemical setup (PCX50C Discover, Perfect Light, Beijing) with LED lamp. In a typical process, the experiments were performed in the mixed solution which dissolved photosensitizer and sacrificial reagent, and suspended with catalysts powder following ultrasonic dispersion for 20 min. During the whole reaction, the continuous magnetic stirring was performed to maintain the evenly dispersed of the reaction mixture. Prior to irradiation, the system was deaerated by bubbling nitrogen for 20 min to eliminate the influence of air. The generated hydrogen was sampled (300  $\mu\text{L}$ ) and then analyzed using gas chromatography (Agilent Technology 7820 A, nitrogen carrier) equipped with thermal conductivity detector (TCD). The catalytic stability was evaluated by isolating, washing and reusing the catalyst in a cycling test. To detect the wavelength dependence of the photocatalytic system, the apparent quantum efficiency (AQE) for HER was analyzed with different band-pass monochromatic filters (420, 435, 450, 475, 500, 520, and 550 nm). The AQE can be calculated by according to the equation (incident photons was obtained by applying the radiant power energy meter):

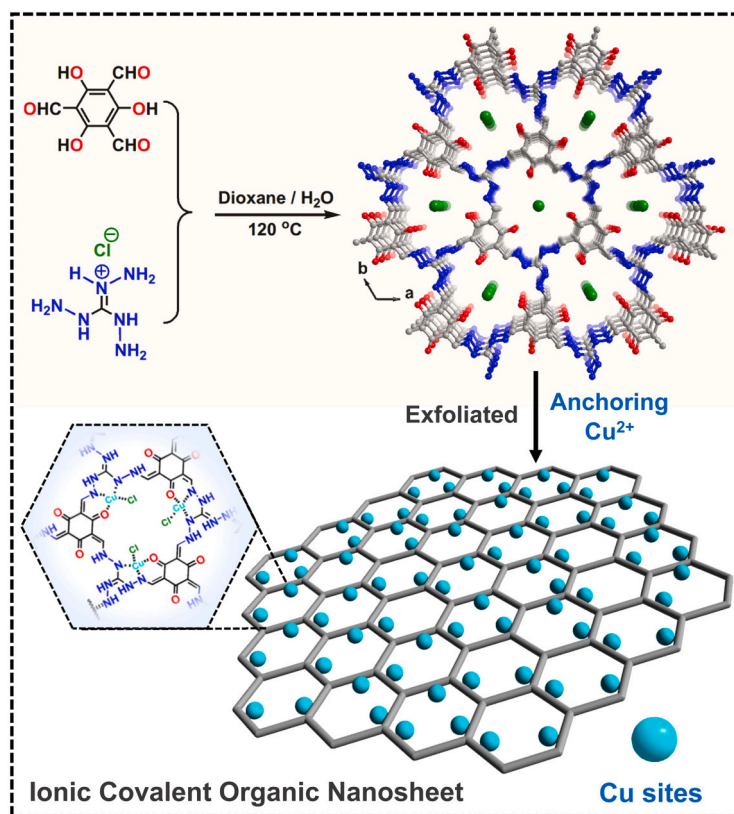
$$\text{AQE} = \frac{2 \times \text{the number of } \text{H}_2 \text{ molecules}}{\text{the number of incident photons}} \times 100\%$$

## 3. Results and discussion

### 3.1. Synthesis and characterization of TpTG-iCON

First, the iCONs were prepared by the improved solvothermal method according to the reported literature [28]. A mixture of 1,3,5-triformylphloroglucinol and triaminoguanidinium chloride (the detailed procedure for Tp and TG is described in the Supporting Information) in a mixed solvent of 1,4-dioxane and deionized water was sonicated for 15 min, and then an acetic acid solution was added to the suspension at room temperature. Subsequently, the mixture was sealed and heated at  $120^\circ\text{C}$  for 72 h (Scheme 1). Powder X-ray diffraction (PXRD) was carried out to verify the crystallinity of the as-synthesized materials. As shown in Fig. 1a, the experimental PXRD profile of the TpTG-iCON material is in agreement with the simulated pattern in terms of diffraction positions [28].

The relatively weak peak at approximately  $10^\circ$  corresponds to the (100) plane. The presence of the (001) plane in the bulk TpTG-iCON



**Scheme 1.** Schematic illustration of the preparation of the Cu@TpTG-iCON.

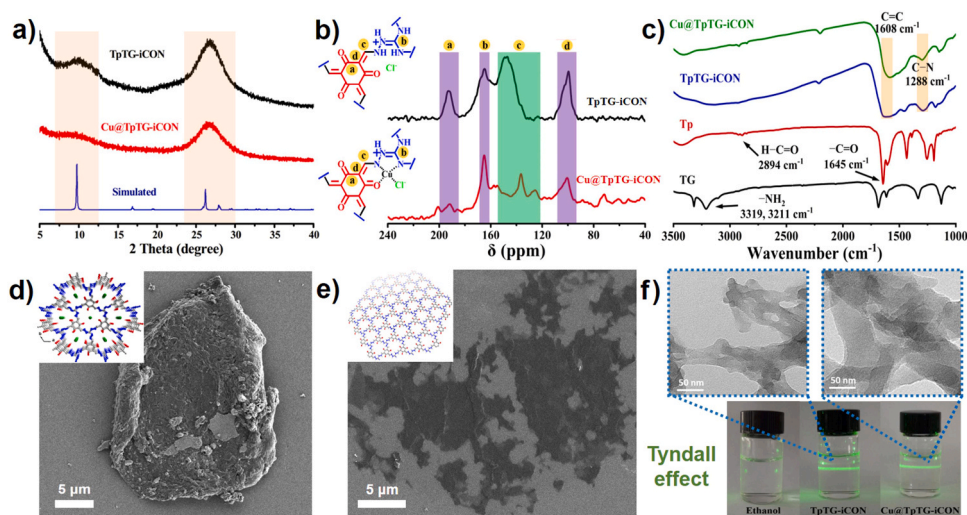


**Fig. 1.** a) PXRD patterns, b)  $^{13}\text{C}$  CP-MAS solid-state NMR spectra, c) FT-IR spectra of TpTG-iCON and Cu@TpTG-iCON. SEM images of d) the bulk TpTG material and e) the exfoliated TpTG-iCON materials. f) The Tyndall effect is observed in solutions of TpTG-iCON and Cu@TpTG-iCON; the inset shows the corresponding TEM images.

material at  $\sim 27^\circ$  indicates that the periodic stacking of 2D layers is extended to the third dimension [31]. The major broad peak indicates fragile  $\pi - \pi$  stacking interactions between the vertically stacked 2D layers in the TpTG-iCON structure, which is due to the intercalation of chloride ions into the assembly of cationic covalent organic nanosheets and charge repulsion between the inbuilt ionic layers, leading to poor crystallinity. Cu@TpTG-iCON is simply obtained by R.T. stirring of a dispersed TpTG-iCON solution with a copper salt (Scheme 1). The colour of the resultant Cu@TpTG-iCON sample changes significantly from yellowish-brown to dark brown. As shown in Fig. 1a, the unchanged

PXRD pattern of Cu@TpTG-iCON indicates that the metalized hybrid material maintains a slice structure similar to that of the initial TpTG-iCON.

Additionally, the structural composition of TpTG-iCON was further confirmed by  $^{13}\text{C}$  cross-polarization magic angle spinning (CP-MAS) NMR spectroscopy. As shown in Fig. 1b, the spectrum shows a characteristic peak at 164 ppm attributed to the C=N carbon in the TG section. In addition, the spectrum shows a distinct signal corresponding to the exocyclic C=C carbon ( $\delta \approx 100$  ppm) adjacent to the C=O carbon [28, 32], together with a characteristic signal of the keto carbon (C=O) at



~190 ppm. The apparent peak at 149 ppm represents the deshielded C=C carbon attached to nitrogen, which supports the formation of an imine moiety in TpTG-iCON. The imine linkages in TpTG-iCON and the metalized Cu@TpTG-iCON material were further investigated by FT-IR spectroscopy. As shown in Fig. 1c, the FT-IR spectrum of the as-synthesized TpTG-iCON shows characteristic stretching frequencies of  $1288\text{ cm}^{-1}$  (C–N) and  $1608\text{ cm}^{-1}$  (C=C) (Fig. 1c). Simultaneously, the characteristic carbonyl stretching band ( $\sim 2894\text{ cm}^{-1}$ ) of the Tp monomer and the primary amine stretching band ( $\sim 3211\text{ cm}^{-1}$ ) of the TG monomer disappeared together, confirming the formation of the proposed imine-linked moiety. The Cu@TpTG-iCON shows an overall similar FT-IR signal, indicating linkages are identical to those in the TpTG-iCON precursor. In addition, an observable blueshift is observed in the spectra of Cu@TpTG-iCON for the C–N stretching vibration ( $1297\text{ cm}^{-1}$ ) compared to the C–N stretching vibration ( $1288\text{ cm}^{-1}$ ) of TpTG-iCON, which may be due to the coordination of the metal ions within the chelation sites [32]. Moreover, after anchoring copper ions, the shielded C=C carbon of Cu@TpTG-iCON has a certain degree of negative shift (Fig. 1b), which may also be a result of the interactions between TpTG-iCON and coordinated copper ions.

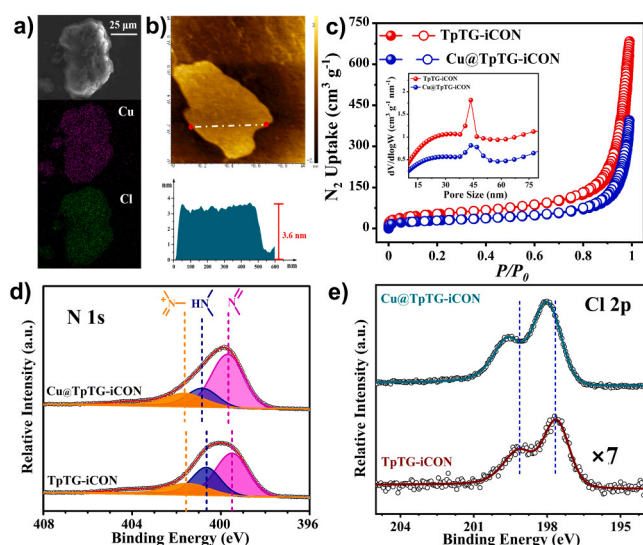
The morphologies of TpTG-iCON and Cu@TpTG-iCON were investigated by scanning electron microscopy (SEM) and transmission electron microscopy (TEM). The bulk TpTG material reveals stacking of overlapping slices (Fig. 1d). Furthermore, the TpTG-iCON sample peeled apart by the ultrasonic treatment exhibits a discontinuous flake morphology composed of flakes with several micrometre lateral dimensions (Fig. 1e and Fig. S1). As shown in Fig. S2, the transmission electron microscopy (TEM) images confirm the porous layer aggregate of TpTG-iCON with abundant clearly visible flaky wrinkles (Fig. S1). After loading copper ions through chelation, Cu@TpTG-iCON still maintains the stacked structure of porous sheets (Fig. S2). Fig. 1f shows the transparent ethanol dispersions of TpTG-iCON and Cu@TpTG-iCON that remain stable for one month, demonstrating the apparent Tyndall effect and indicating that the formed covalent organic nanosheets are uniformly dispersed. Typically, the resulting Cu@TpTG-iCON substantially retains the original morphology of the TpTG nanosheets. The EDS elemental mapping images confirm the uniform distribution of Cu sites across the entire aggregate (Fig. 2a and Fig. S3). The ultrathin nanosheet morphologies of TpTG-iCON and Cu@TpTG-iCON are also supported by the TEM and atomic force microscopy (AFM) images (Fig. 2b and

Fig. S4). The AFM image indicates that TpTG-iCON exists as typical discontinuous slices with a thickness of  $\sim 3.3\text{ nm}$  (Fig. S4). Additionally, Cu@TpTG-iCON still maintains a thickness of  $\sim 3.6\text{ nm}$  (Fig. 2b), which demonstrates that the loading of copper ions does not cause the aggregation of covalent organic nanosheets. The fully exfoliated lamellar architecture of Cu@TpTG-iCON will make almost all active sites on the surface available to substrates and reagents without diffusion limitations, which will greatly increase the reaction kinetics during the photocatalytic HER process.

Nitrogen adsorption-desorption measurements at 77 K of the TpTG-iCON and Cu@TpTG-iCON materials were examined to investigate the specific surface area and porous nature. As shown in Fig. 2c, the  $\text{N}_2$  adsorption-desorption isotherm of TpTG-iCON exhibits the typical characteristics of type II reversible isotherms [33]. After chelating copper ions, Cu@TpTG-iCON exhibits similar adsorption-desorption characteristics, accompanied by a slight decrease in adsorption capacity. The corresponding Brunauer-Emmett-Teller (BET) specific surface areas are  $189$  and  $105\text{ m}^2\text{ g}^{-1}$  for TpTG-iCON and Cu@TpTG-iCON, respectively. The lower surface area of TpTG-iCON can be attributed to weaker layer stacking and pore blocking by the counteranions [28]. Simultaneously, the significantly decreased BET area and porosity of Cu@TpTG-iCON arise from the introduction of heavier Cu atoms coordinated by polydentate ligands of the TpTG-iCON precursor (Fig. 2c and Table S1). The loading of Cu is approximately 9.5 wt% in the TpTG-iCON host, as determined by ICP-MS.

X-ray photoelectron spectroscopy (XPS) was utilized to analyse the detailed surface chemical states of the TpTG-iCON and Cu@TpTG-iCON materials. The presence of C, N, O, and Cl is confirmed in the full survey XPS spectra of TpTG-iCON (Fig. S5a). Furthermore, the spectrum of Cu@TpTG-iCON contains an additional signal of Cu and an enhanced peak of Cl 2p compared with that of the TpTG-iCON matrix (Fig. S5b), indicating that the copper species are successfully incorporated into the TpTG-iCON substance. Fig. S6a shows the high-resolution XPS spectrum of copper, the apparent asymmetrical Cu  $2p_{3/2}$  and Cu  $2p_{1/2}$  peaks indicate the mixed-valence Cu in the materials [34]. Additionally, two strong satellite signals ( $944.0\text{ eV}$  and  $963.9\text{ eV}$ ) are observed next to the Cu  $2p_{3/2}$  and Cu  $2p_{1/2}$  peaks, respectively, indicating the dominant presence of Cu(II) ions anchored in TpTG-iCON matrix. Furthermore, the high-resolution XPS spectra can be fitted well by three sets of peaks (Fig. S6b), which can be classified as the presence of different bonding for Cu–O, Cu–Cl, and Cu–N in the Cu@TpTG-iCON. As shown in Fig. 2d, the high-resolution N 1s XPS spectra of TpTG-iCON are deconvoluted to reveal three types of nitrogen species. The peaks at  $399.5$ ,  $400.6$ , and  $401.5\text{ eV}$  are attributed to imine nitrogen, secondary amine nitrogen, and quaternary positively charged nitrogen species, respectively [35]. Notably, the deconvoluted N 1s peak of Cu@TpTG-iCON clearly shows three types of N species, similar to the results for TpTG-iCON, while these peaks both demonstrate a significant positive shift compared with those of the initial TpTG-iCON matrix (Fig. 2d). This may be due to the coordinated interaction between copper ions and the donated nitrogen sites, which affects the electronic structure of these nitrogen species [36].

Similar peaks also appeared in the O 1s spectrum (Fig. S7), and the high-resolution fitted O 1s spectra of TpTG-iCON demonstrate three types of O species, namely, C–O ( $531.0\text{ eV}$ ), C=O ( $532.8\text{ eV}$ ), and C–OH ( $535.7\text{ eV}$ ) [37]. As shown in Fig. S7, the C–OH peak almost disappeared, accompanied by the positive shift of the C–O and C=O peaks after chelating Cu, which may be a result of the deprotonation of phenolic hydroxyl groups as coordinating with Cu ions. In addition, compared with that of TpTG-iCON, the content of Cl in Cu@TpTG-iCON significantly increases from 0.3 to 2.2 (atomic %). Correspondingly, the XPS signal of chlorine is significantly enhanced (Fig. S5 and Fig. 2e), which indicates that the introduction of copper ions is accompanied by the combination of a large number of chloride ions. As shown in Fig. 2e, the Cl 2p peak of Cu@TpTG-iCON also shifted significantly relative to that of the initial TpTG-iCON, which is most likely due to the binding of



**Fig. 2.** a) EDS elemental mapping of Cu@TpTG-iCON. b) AFM image and the corresponding height value of Cu@TpTG-iCON. c)  $\text{N}_2$  adsorption isotherms measured at 77 K and pore size distribution profiles of TpTG-iCON and Cu@TpTG-iCON. High-resolution N 1s d) and Cl 2p e) XPS spectra of TpTG-iCON and Cu@TpTG-iCON.

chloride ions to the copper centre via coordinative interactions. In summary, all the above results verify the structure of the multidentate chelating moiety anchoring the active copper sites. Detached ionic covalent-organic nanosheets anchoring dispersed copper ions as quasi-homogeneous catalysts were successfully fabricated, which can enhance the surface-to-volume ratio to maximize the exposure of active metal sites and improve the HER performance during the catalytic process.

### 3.2. Photocatalytic hydrogenation

Because of these structural advantages, the photocatalytic HER performance of Cu@TpTG-iCON as a proton reduction catalyst was investigated in a ternary system. First, the effect of a photosensitizer (PS) and sacrificial agent (SA) on the photocatalytic performance of the system was examined to obtain the best catalytic activity (Fig. S8). The results demonstrate that the Cu@TpTG-iCON catalyst exhibits the best photocatalytic HER performance when fluorescein is used as a photosensitizer and TEA is used as an electron donor. Furthermore, control experiments revealed that no hydrogen is produced in the absence of individual components (Cu@TpTG-iCON, photosensitizer, and sacrificial reductant) or in the dark, which indicates that all materials are essential for photocatalytic hydrogen generation. In addition, the solvent environment has a dramatic effect on the performance of artificial photosynthetic systems [38]. Fig. S9 shows the effect of different solvent systems on the photocatalytic HER performance. Cu@TpTG-iCON demonstrates the best hydrogen evolution rate of  $\sim 8 \text{ mmol g}^{-1} \text{ h}^{-1}$  in  $\text{H}_2\text{O}/\text{DMAc}$  medium ( $V:V = 1:1$ , detailed in Fig. S10), which may be due to multiple factors, including solvent polarity, solvent coordination ability, and different solvent dielectric constants [39].

Additionally, the photocatalytic HER performance is significantly affected by the PS and SA concentrations, and the optimal photocatalytic parameters were determined based on these results (Figs. S11 and S12). Moreover, to examine the dependence of the HER activity on the catalyst concentration, photocatalytic tests were executed by dispersing various amounts of Cu@TpTG-iCON into the photocatalytic system under illumination. The catalytic HER efficiency approached the optimal value under lower catalyst concentrations ( $0.05 \text{ mg/mL}$ ) in the photocatalytic system (Fig. S13). Under higher catalyst concentrations in this artificial photosynthetic system, the lower hydrogen production activity may be due to the formed turbid system that inhibits the absorption of incident light by obstructing the light path [40]. More importantly, the TpTG-iCON precursor with a similar nanosheet structure exhibits extremely low catalytic activity for proton reduction (Fig. 3a). In contrast, the Cu@TpTG-iCON demonstrates greatly enhanced photocatalytic HER performance ( $\sim 8 \text{ mmol g}^{-1} \text{ h}^{-1}$ ) under the same conditions, being significantly superior to most of the reported COF-based systems even including Pt co-catalyst (Table S2), which also indicates that the dispersed Cu species are well proposed as the real active sites for catalytic proton reduction. Homogeneous catalysis demonstrates obvious advantages with regard to accessible active sites [41]. Meanwhile, the catalytic performance of Cu@TpTG-Bulk is significantly attenuated to  $\sim 50\%$  of Cu@TpTG-iCON (Fig. 3a), which is due to the loss of accessible active Cu sites. The Cu@TpTG-iCON with a thin nanosheet structure can expose more catalytic sites and accelerates the transmission of electrons at the interface, endowing Cu@TpTG-iCON with obvious quasi-homogeneous advantages for photocatalytic proton reduction. As shown in Fig. 3b, Cu@TpTG-iCON is recycled for three runs without considerable changes in the photocatalytic HER performance. The few-layered nanosheet structure can maximize the exposure of catalytic sites to improve the accessibility of metal centres, making it a reusable quasi-homogeneous catalyst. Fig. 3c shows the wavelength-dependent apparent quantum efficiency (AQE) of Cu@TpTG-iCON in the photocatalytic system. The highest calculated AQE value at 450 nm reaches 0.33% and decreases to 0.25% and 0.09% at 475 nm and 500 nm, respectively. As shown in Fig. S14, the porous

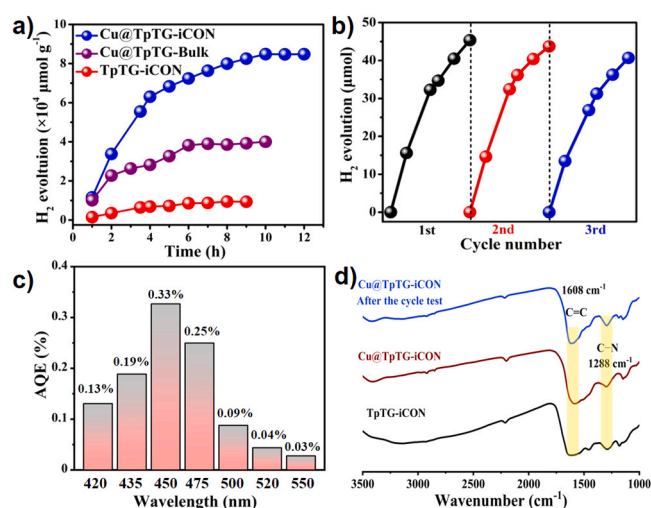


**Fig. 3.** a) Hydrogen evolution performance of TpTG-iCON, Cu@TpTG-Bulk, and Cu@TpTG-iCON. b) cycling photocatalytic HER test for Cu@TpTG-iCON. c) wavelength-dependent apparent quantum efficiency (AQE) of Cu@TpTG-iCON in the optimized system. d) FT-IR spectra of the Cu@TpTG-iCON after the cycling tests.

nanosheets morphology of Cu@TpTG-iCON is maintained well after photocatalytic experiments. Moreover, the Cu@TpTG-iCON slice after the photocatalytic HER test still remains a few-layered nanosheet thickness of  $\sim 3.6 \text{ nm}$  (Fig. S14c), which both verified the strong stability of Cu@TpTG-iCON nanosheets. Furthermore, the FT-IR spectrum of Cu@TpTG-iCON after photocatalysis still shows characteristic stretching frequencies of  $1288 \text{ cm}^{-1}$  (C—N) and  $1608 \text{ cm}^{-1}$  (C=C), which originate from the skeleton of iCON, indicating preferable structural stability of the covalent-organic matrix (Fig. 3d). Additionally, the EDS elemental analysis result confirms that there is no copper element in the filtrate after the photocatalytic experiment (Fig. S15), implying the negligible leaching of  $\text{Cu}^{2+}$  during the photocatalytic reaction, which may be attributed to the strong chelated coordination interaction between polydentate chelation vacancies and copper ions.

### 3.3. Mechanism proposed

Furthermore, we carried out photoluminescence (PL) spectroscopy and time-resolved photoluminescence (TRPL) to illustrate the mechanism of photogenerated carrier transfer and separation in this photocatalytic system. First, in view of that, the fluorescein can exist in different species with dissimilar photophysical properties depending on the system pH [42], the FL-blank control was obtained by adding the same equivalent of NaOH as TEA into the initial FL solution to subtract the interference. As shown in Fig. 4a, the FL-Blank solution shows a strong PL single emission at 540 nm, which corresponds to the electronic excitation from the highest occupied molecular orbital of FL dianion to the lowest unoccupied molecular orbital [42]. When the real catalytic concentration of Cu@TpTG-iCON coexists with the FL-blank solution, the emission intensity is attenuated significantly, indicating a strong quenching between dispersed Cu@TpTG-iCON nanosheets and excited FL\*. In other words, the electron-hole recombination rate is obviously suppressed by Cu@TpTG-iCON, meaning that Cu@TpTG-iCON can greatly promote the electron transport for improving the charge separation efficiency in this photocatalytic system. In contrast, when 10% TEA is introduced into the FL-blank the emission intensity of FL\* is quenched by 51%, which is far exceeding that of Cu@TpTG-iCON quencher. Fig. 4b shows the corresponding time-resolved photoluminescence, in the FL-Blank, the lifetime of the excited FL\* is 5.65 ns. When Cu@TpTG-iCON or TEA is introduced into the initial solution, the corresponding lifetime of the FL\* is extended to 6.83 and 6.90 ns,

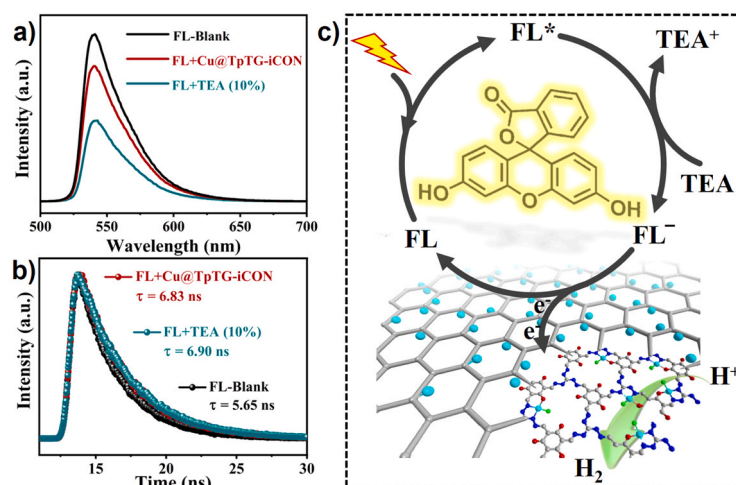


**Fig. 4.** a) Emission spectra of FL solution upon addition of Cu@TpTG-iCON and TEA in the mimic real photocatalytic condition. b) The corresponding TRPL lifetime decay curves. c) The proposed mechanism of photocatalytic HER in the fluorescein-sensitized Cu@TpTG-iCON system.

respectively, indicating that the presence of either Cu@TpTG-iCON or TEA can effectively prolong the lifetime of FL\*, which is conducive to the photocatalytic proton reduction [43].

Regarding the initial photochemical step, the electron-transfer quenching of FL\* is possible in two ways: either reductive quenching by TEA or oxidative quenching by Cu@TpTG-iCON catalyst. To examine the photochemically driven electron-transfer steps of the ternary photocatalytic system (FL/Cu@TpTG-iCON/TEA) in more detail, the FL\* quenching experiments were carried out with Cu@TpTG-iCON catalyst and TEA, respectively. As shown in Fig. S16 and Fig. S17, the fluorescence intensity of FL decreases gradually with the increase of Cu@TpTG-iCON and TEA, demonstrating the efficient electron-transfer between FL and quencher. The FL\* quenching constant  $K_{SV}$  was determined to be  $0.33 \text{ M}^{-1}$  from the linear fitting of the Stern-Volmer plot for TEA. Meanwhile, the Cu@TpTG-iCON catalyst quenches the fluorescence of FL with a quenching constant  $K_{SV}$  ( $3.23 \times 10^3 \text{ M}^{-1}$ ). However, although the oxidative quenching constant by Cu@TpTG-iCON is more than four orders of magnitude larger than that of the reductive quenching constant by TEA, the concentration of electron donor TEA (0.72 M) is much higher than that of Cu@TpTG-iCON (ca.  $10^{-5} \text{ M}$ ) in the real photocatalytic condition. Furthermore, given the homogeneous quenching of TEA molecular and the heterogeneous quenching of Cu@TpTG-iCON for FL respectively, we believe that reduction quenching (TEA for photosensitizer FL) dominates in the initial electron transfer process [13,44,45]. Therefore, a possible pathway of photocatalytic proton reduction is shown in Fig. 4c. Upon light irradiation, the photon is first absorbed by the photosensitizer FL to generate the excited FL\*, which is rapidly reduced by the TEA molecule to form FL<sup>-</sup> with strong reducing ability. Afterward, FL<sup>-</sup> transfers the electrons on the scattered Cu@TpTG-iCON catalyst to trigger the photochemical proton reduction reaction that occurs at dispersed active copper species.

#### 4. Conclusions

In summary, the construction strategy of a recyclable quasi-homogeneous catalyst of ionic covalent organic nanosheets anchoring dispersed Cu atoms and exhibiting outstanding photocatalytic H<sub>2</sub> generation was proposed and studied. The TpTG-iCON prefabricated with evenly dispersed tridentate chelation sites can easily bind free copper(II) ions to form the hybrid Cu@TpTG-iCON. Cu@TpTG-iCON can be easily peeled off to form a scattered nanosheet, which can maximize the exposure of active sites during the catalytic reaction. Taking advantage of the well-defined structural configuration and nanosheet morphology, the heterogeneous Cu@TpTG-iCON catalyst exhibits an excellent high

HER rate of  $8484 \mu\text{mol g}^{-1} \text{ h}^{-1}$  under a ternary photocatalytic system along with the significant stability. More importantly, the strategy of prefabricating anchor sites in covalent organic nanosheet matrix successfully demonstrated here is a new method to synthesize other non-precious metal-based hybrid iCON materials, which is a step forward in the development of recyclable and efficient HER catalysts.

#### CRediT authorship contribution statement

**Ying Zang:** Investigation, Methodology, Writing – original draft. **Yuan-Jie Cheng:** Methodology, Data curation. **Zhao-Di Wang:** Methodology, Data curation. **Peng Peng:** Investigation, Validation. **Qing-Guo Dong:** Methodology, Data curation. **Hong Chen:** Methodology, Data curation. **Rui Wang:** Supervision, Conceptualization, Writing – review & editing. **Shuang-Quan Zang:** Conceptualization, Supervision, Project administration, Funding acquisition, Writing – review & editing.

#### Declaration of Competing Interest

The authors declare that they have no known competing financial interests or personal relationships that could have appeared to influence the work reported in this paper.

#### Acknowledgements

This work was supported by the National Natural Science Foundation of China (No. 92061201, 21825106, 22001236), the Program for Innovative Research Team (in Science and Technology) in Universities of Henan Province (19IRTSTHN022) and Zhengzhou University.

#### Appendix A. Supporting information

Supplementary data associated with this article can be found in the online version at [doi:10.1016/j.apcatb.2021.120817](https://doi.org/10.1016/j.apcatb.2021.120817).

#### References

- [1] Z. Wang, C. Li, K. Domen, Recent developments in heterogeneous photocatalysts for solar-driven overall water splitting, *Chem. Soc. Rev.* 48 (2019) 2109–2125.
- [2] Q. Yang, M. Luo, K. Liu, H. Cao, H. Yan, Covalent organic frameworks for photocatalytic applications, *Appl. Catal. B-Environ.* 276 (2020), 119174.
- [3] X. Ma, L. Wang, Q. Zhang, H.-L. Jiang, Switching on the photocatalysis of metal-organic frameworks by engineering structural defects, *Angew. Chem. Int. Ed.* 58 (2019) 12175–12179.
- [4] J. Fu, B. Zhu, W. You, M. Jaroniec, J. Yu, A flexible bio-inspired H<sub>2</sub>-production photocatalyst, *Appl. Catal. B-Environ.* 220 (2018) 148–160.



- [5] L. Jiang, X. Yuan, Y. Pan, J. Liang, G. Zeng, Z. Wu, H. Wang, A novel method of adrenal venous sampling via an antecubital approach, *Appl. Catal. B-Environ.* 217 (2017) 388–406.
- [6] H. Zhang, P. Zhang, M. Qiu, J. Dong, Y. Zhang, X.-W. Lou, Ultrasmall MoO<sub>x</sub> clusters as a novel cocatalyst for photocatalytic hydrogen evolution, *Adv. Mater.* 31 (2019), 1804883.
- [7] Y. Zang, J. Zhang, R. Wang, Z.-D. Wang, Y. Zhu, X. Ren, S. Li, X.-Y. Dong, S.-Q. Zang, Inter-chain double-site synergistic photocatalytic hydrogen evolution in robust cuprous coordination polymers, *Chem. Commun.* 56 (2020) 6261–6264.
- [8] A. López-Magano, A.E. Platero-Prats, S. Cabrera, R. Mas-Ballesté, J. Alemán, Incorporation of photocatalytic Pt(II) complexes into imine-based layered covalent organic frameworks (COFs) through monomer truncation strategy, *Appl. Catal. B-Environ.* 272 (2020), 119027.
- [9] D. Shi, R. Zheng, M.-J. Sun, X. Cao, C.-X. Sun, C.-J. Cui, C.-S. Liu, J. Zhao, M. Du, Semiconductive copper(I)-organic frameworks for efficient light-driven hydrogen generation without additional photosensitizers and cocatalysts, *Angew. Chem. Int. Ed.* 56 (2017) 14637–14641.
- [10] M. Wen, K. Mori, Y. Kuwahara, T. An, H. Yamashita, Design and architecture of metal organic frameworks for visible light enhanced hydrogen production, *Appl. Catal. B-Environ.* 218 (2017) 555–569.
- [11] D.J. Woods, S.A.J. Hillman, D. Pearce, L. Wilbraham, L.Q. Flagg, W. Duffy, I. McCulloch, J.R. Durrant, A.A.Y. Guilbert, M.A. Zwijnenburg, R.S. Sprick, J. Nelson, A.I. Cooper, Side-chain tuning in conjugated polymer photocatalysts for improved hydrogen production from water, *Energy Environ. Sci.* 13 (2020) 1843–1855.
- [12] H. Lv, T.P. Ruberu, V.E. Fleischauer, W.W. Brennessel, M.L. Neidig, R. Eisenberg, Catalytic light-driven generation of hydrogen from water by iron dithiolene complexes, *J. Am. Chem. Soc.* 138 (2016) 11654–11663.
- [13] K. Liu, R. Xing, Y. Li, Q. Zou, H. Mohwald, X. Yan, Mimicking primitive photobacteria: sustainable hydrogen evolution based on peptide-porphyrin Co-assemblies with a self-mineralized reaction center, *Angew. Chem. Int. Ed.* 55 (2016) 12503–12507.
- [14] Z. Han, L. Shen, W.W. Brennessel, P.L. Holland, R. Eisenberg, Nickel pyridinethiolate complexes as catalysts for the light-driven production of hydrogen from aqueous solutions in noble-metal-free systems, *J. Am. Chem. Soc.* 135 (2013) 14659–14669.
- [15] X. Chen, S. Xiao, H. Wang, W. Wang, Y. Cai, G. Li, M. Qiao, J. Zhu, H. Li, D. Zhang, Y. Lu, MOFs conferred with transient metal centers for enhanced photocatalytic activity, *Angew. Chem. Int. Ed.* 59 (2020) 17182–17186.
- [16] Y. Xu, N. Mao, C. Zhang, X. Wang, J. Zeng, P. Xu, Y. Chen, F. Wang, J.-X. Jiang, Rational design of donor- $\pi$ -acceptor conjugated microporous polymers for photocatalytic hydrogen production, *Appl. Catal. B-Environ.* 228 (2018) 1–9.
- [17] J. Chen, X. Tao, C. Li, Y. Ma, L. Tao, D. Zheng, J. Zhu, H. Li, R. Li, Q. Yang, Synthesis of bipyridine-based covalent organic frameworks for visible-light-driven photocatalytic water oxidation, *Appl. Catal. B-Environ.* 262 (2020), 118271.
- [18] Y. Zang, R. Wang, P.-P. Shao, X. Feng, S. Wang, S.-Q. Zang, T.C.W. Mak, Prefabricated covalent organic framework nanosheets with double vacancies: anchoring Cu for highly efficient photocatalytic H<sub>2</sub> evolution, *J. Mater. Chem. A* 8 (2020) 25094–25100.
- [19] T. Banerjee, F. Haase, G. Savasci, K. Gottschling, C. Ochsenfeld, B.V. Lotsch, Single-site photocatalytic H<sub>2</sub> evolution from covalent organic frameworks with molecular cobaloxime Co-catalysts, *J. Am. Chem. Soc.* 139 (2017) 16228–16234.
- [20] C. Qian, W. Zhou, J. Qiao, D. Wang, X. Li, W.L. Teo, X. Shi, H. Wu, J. Di, H. Wang, G. Liu, L. Gu, J. Liu, L. Feng, Y. Liu, S.Y. Quek, K.P. Loh, Y. Zhao, Linkage engineering by harnessing supramolecular interactions to fabricate 2D hydrazone-linked covalent organic framework platforms toward advanced catalysis, *J. Am. Chem. Soc.* 142 (2020) 18138–18149.
- [21] W. Chen, L. Wang, D. Mo, F. He, Z. Wen, X. Wu, H. Xu, L. Chen, Modulating benzothiadiazole-based covalent organic frameworks via halogenation for enhanced photocatalytic water splitting, *Angew. Chem. Int. Ed.* 59 (2020) 16902–16909.
- [22] S. Ghosh, A. Nakada, M.A. Springer, T. Kawaguchi, K. Suzuki, H. Kaji, I. Baburin, A. Kuc, T. Heine, H. Suzuki, R. Abe, S. Seki, Identification of prime factors to maximize the photocatalytic hydrogen evolution of covalent organic frameworks, *J. Am. Chem. Soc.* 142 (2020) 9752–9762.
- [23] B.P. Biswal, H.A. Vignolo-Gonzalez, T. Banerjee, L. Grunenberg, G. Savasci, K. Gottschling, J. Nuss, C. Ochsenfeld, B.V. Lotsch, Sustained solar H<sub>2</sub> evolution from a thiazolo[5,4-d]thiazole-bridged covalent organic framework and nickel-thiolate cluster in water, *J. Am. Chem. Soc.* 141 (2019) 11082–11092.
- [24] X. Jiao, K. Zheng, L. Liang, X. Li, Y. Sun, Y. Xie, Fundamentals and challenges of ultrathin 2D photocatalysts in boosting CO<sub>2</sub> photoreduction, *Chem. Soc. Rev.* 49 (2020) 6592–6604.
- [25] X. Li, P. Yadav, K.P. Loh, Function-oriented synthesis of two-dimensional (2D) covalent organic frameworks - from 3D solids to 2D sheets, *Chem. Soc. Rev.* 49 (2020) 4835–4866.
- [26] M. Martínez-Abadía, A. Mateo-Alonso, Structural approaches to control interlayer interactions in 2D covalent organic frameworks, *Adv. Mater.* 32 (2020), 2002366.
- [27] W. Liu, X. Luo, Y. Bao, Y.P. Liu, G.H. Ning, I. Abdelwahab, L. Li, C.T. Nai, Z.G. Hu, D. Zhao, B. Liu, S.Y. Quek, K.P. Loh, A two-dimensional conjugated aromatic polymer via C-C coupling reaction, *Nat. Chem.* 9 (2017) 563–570.
- [28] S. Mitra, S. Kandambeth, B.P. Biswal, M.A. Khayum, C.K. Choudhury, M. Mehta, G. Kaur, S. Banerjee, A. Prabhune, S. Verma, S. Roy, U.K. Kharul, R. Banerjee, Self-exfoliated guanidinium-based ionic covalent organic nanosheets (iCONs), *J. Am. Chem. Soc.* 138 (2016) 2823–2828.
- [29] J. Tan, S. Namuangruk, W.F. Kong, N. Kungwan, J. Guo, C.C. Wang, Manipulation of amorphous-to-crystalline transformation: towards the construction of covalent organic framework hybrid microspheres with NIR photothermal conversion ability, *Angew. Chem. Int. Ed.* 55 (2016) 13979–13984.
- [30] Y.-H. Gong, F. Miomandre, R. Méallet-Renault, S. Badré, L. Galmiche, J. Tang, P. Audebert, G. Clavier, Synthesis and physical chemistry of s-tetrazines: which ones are fluorescent and why? *Eur. J. Org. Chem.* 35 (2009) 6121–6128.
- [31] Y. Peng, Y. Huang, Y. Zhu, B. Chen, L. Wang, Z. Lai, Z. Zhang, M. Zhao, C. Tan, N. Yang, F. Shao, Y. Han, H. Zhang, Ultrathin two-dimensional covalent organic framework nanosheets: preparation and application in highly sensitive and selective DNA detection, *J. Am. Chem. Soc.* 139 (2017) 8698–8704.
- [32] S. Kandambeth, A. Mallick, B. Lukose, M.V. Mane, T. Heine, R. Banerjee, Construction of crystalline 2D covalent organic frameworks with remarkable chemical (acid/base) stability via a combined reversible and irreversible route, *J. Am. Chem. Soc.* 134 (2012) 19524–19527.
- [33] K.A. Cychosz, R. Guillet-Nicolas, J. Garcia-Martinez, M. Thommes, Recent advances in the textural characterization of hierarchically structured nanoporous materials, *Chem. Soc. Rev.* 46 (2017) 389–414.
- [34] B. Tu, Q. Pang, H. Xu, X. Li, Y. Wang, Z. Ma, L. Weng, Q. Li, Reversible redox activity in multicomponent metal-organic frameworks constructed from trinuclear copper pyrazolate building blocks, *J. Am. Chem. Soc.* 139 (2017) 7998–8007.
- [35] Y.-J. Cheng, R. Wang, S. Wang, X.-J. Xi, L.-F. Ma, S.-Q. Zang, Encapsulating [Mo<sub>3</sub>S<sub>13</sub>]<sup>2-</sup> clusters in cationic covalent organic frameworks: enhancing stability and recyclability by converting a homogeneous photocatalyst to a heterogeneous photocatalyst, *Chem. Commun.* 54 (2018) 13563–13566.
- [36] L. Ma, W. Hu, B. Mei, H. Liu, B. Yuan, J. Zang, T. Chen, L. Zou, Z. Zou, B. Yang, Y. Yu, J. Ma, Z. Jiang, K. Wen, H. Yang, Covalent triazine framework confined copper catalysts for selective electrochemical CO<sub>2</sub> reduction: operando diagnosis of active sites, *ACS Catal.* 10 (2020) 4534–4542.
- [37] C. Zhao, S. Zhang, M. Han, X. Zhang, Y. Liu, W. Li, C. Chen, G. Wang, H. Zhang, H. Zhao, Ambient electrosynthesis of ammonia on a biomass-derived nitrogen-doped porous carbon electrocatalyst: contribution of pyridinic nitrogen, *ACS Energy Lett.* 4 (2019) 377–383.
- [38] Y. Lei, M. Yang, J. Hou, F. Wang, E. Cui, C. Kong, S. Min, Thiomolybdate [Mo<sub>3</sub>S<sub>13</sub>]<sup>2-</sup> nanocluster: a molecular mimic of MoS<sub>2</sub> active sites for highly efficient photocatalytic hydrogen evolution, *Chem. Commun.* 54 (2018) 603–606.
- [39] P. Du, J. Schneider, G. Luo, W.W. Brennessel, R. Eisenberg, Visible light-driven hydrogen production from aqueous protons catalyzed by molecular cobaloxime catalysts, *Inorg. Chem.* 48 (2009) 4952–4962.
- [40] K.K. Mandari, N. Son, Y.S. Kim, M. Kang, Plasmonic quaternary heteronanostructures (HNSs) for improved solar light utilization, spatial charge separation, and stability in photocatalytic hydrogen production, *J. Colloid Interface Sci.* 582 (2021) 720–731.
- [41] C. Huang, J. Wen, Y. Shen, F. He, L. Mi, Z. Gan, J. Ma, S. Liu, H. Ma, Y. Zhang, Dissolution and homogeneous photocatalysis of polymeric carbon nitride, *Chem. Sci.* 9 (2018) 7912–7915.
- [42] N.O. Mchedlov-Petrosyan, T.A. Chepesh, A.D. Roshal, S.V. Shekhovtsov, E. G. Moskaeva, I.V. Omelchenko, Aminofluoresceins versus fluorescein: peculiarity of fluorescence, *J. Phys. Chem. A* 123 (2019) 8860–8870.
- [43] Z. Jin, Y. Zhang, Q. Ma, Orthorhombic WP co-catalyst coupled with electron transfer bridge UiO-66 for efficient visible-light-driven H<sub>2</sub> evolution, *J. Colloid Interface Sci.* 556 (2019) 689–703.
- [44] Z. Han, W.R. McNamara, M.S. Eum, P.L. Holland, R. Eisenberg, A nickel thiolate catalyst for the long-lived photocatalytic production of hydrogen in a noble-metal-free system, *Angew. Chem. Int. Ed.* 51 (2012) 1667–1670.
- [45] Z.-D. Wang, Y. Zang, Z.-J. Liu, P. Peng, R. Wang, S.-Q. Zang, Opening catalytic sites in the copper-triazoles framework via defect chemistry for switching on the proton reduction, *Appl. Catal. B-Environ.* 288 (2021), 119941.